

## Research Paper

# Chelator-Free Radiolabeling of SERRS Nanoparticles for Whole-Body PET and Intraoperative Raman Imaging

Matthew A. Wall<sup>1,2\*</sup>, Travis M. Shaffer<sup>1,2\*</sup>, Stefan Harmsen<sup>1</sup>, Darjus-Felix Tschaharganeh<sup>3</sup>, Chun-Hao Huang<sup>3</sup>, Scott W. Lowe<sup>3,4</sup>, Charles Michael Drain<sup>2</sup>, and Moritz F. Kircher<sup>1,5,6,7</sup>✉

1. Department of Radiology, Memorial Sloan Kettering Cancer Center, New York, NY, USA;
2. Department of Chemistry, Hunter College and the Graduate Center, City University of New York, New York, NY, USA;
3. Cancer Biology and Genetics Program, Memorial Sloan Kettering Cancer Center, New York, NY, USA;
4. Howard Hughes Medical Institute, New York, NY, USA;
5. Center for Molecular Imaging and Nanotechnology (CMINT), Memorial Sloan Kettering Cancer Center, New York, NY, USA;
6. Molecular Pharmacology Program, Sloan Kettering Institute, Memorial Sloan Kettering Cancer Center, New York, NY, USA;
7. Department of Radiology, Weill Cornell Medical College of Cornell University, New York, NY, USA.

\* These authors contributed equally to this work.

✉ Corresponding author: E-mail: kircher@mskcc.org

© Ivyspring International Publisher. This is an open access article distributed under the terms of the Creative Commons Attribution (CC BY-NC) license (<https://creativecommons.org/licenses/by-nc/4.0/>). See <http://ivyspring.com/terms> for full terms and conditions.

Received: 2016.12.20; Accepted: 2017.05.17; Published: 2017.07.22

## Abstract

A single contrast agent that offers whole-body non-invasive imaging along with the superior sensitivity and spatial resolution of surface-enhanced resonance Raman scattering (SERRS) imaging would allow both pre-operative mapping and intraoperative imaging and thus be highly desirable. We hypothesized that labeling our recently reported ultrabright SERRS nanoparticles with a suitable radiotracer would enable pre-operative identification of regions of interest with whole body imaging that can be rapidly corroborated with a Raman imaging device or handheld Raman scanner in order to provide high precision guidance during surgical procedures. Here we present a straightforward new method that produces radiolabeled SERRS nanoparticles for combined positron emission tomography (PET)-SERRS tumor imaging without requiring the attachment of molecular chelators. We demonstrate the utility of these PET-SERRS nanoparticles in several proof-of-concept studies including lymph node (LN) tracking, intraoperative guidance for LN resection, and cancer imaging after intravenous injection. We anticipate that the radiolabeling method presented herein can be applied generally to nanoparticle substrates of various materials by first coating them with a silica shell and then applying the chelator-free protocol.

Key words: Intrinsic radiolabeling, Surface-enhanced resonance Raman scattering, SERS, Positron emission tomography, *in vivo*, Imaging.

## Introduction

High-precision intraoperative imaging is necessary to delineate the true extent of tumor borders and identify the presence of multiple cancer foci or micrometastases. Failure to remove these malignant cells is a major reason for local recurrences and metastatic spread [1]. We previously demonstrated that the new generations of surface-enhanced resonance Raman scattering (SERRS) nanoparticles we have developed enable the visualization of the exact extent of malignant and even premalignant lesions after intravenous injection in many different mouse models, with microscopic

accuracy [2-10]. Unlike conventional fluorescent imaging agents, SERRS nanoparticles exhibit exceptionally low limits of detection, resistance to photobleaching, unambiguous spectral signatures, and high multiplexing capabilities [2-4]. There is an increasing interest in gold nanoparticles as a platform for cancer marker detection [11]. Our recently reported surfactant-free synthesis method of the gold nanoparticle cores should further aid in developing nontoxic SERRS nanoparticles with the potential for clinical translation [12, 13]. In contrast to fluorescence imaging agents [14], the unique

spectrum of SERRS nanoparticles does not exist *in vivo* and its specificity is therefore not affected by autofluorescence. The SERRS spectra serve as molecular fingerprints for optical imaging with very high signal-to-background ratios [7]. After resection under white-light, we were able to show that residual cancer can be visualized with SERRS imaging with tumor deposits as small as 100  $\mu\text{m}$  being detectable, thereby minimizing the risk that cancer is left behind during surgery [4, 9, 15]. The increased precision of imaging the true extent of cancerous spread could markedly reduce the need for unnecessary resection of surrounding healthy tissue. It could also enable surgeries that are presently deemed unfeasible due to the proximity of adjacent crucial structures such as nerves or blood vessels, and allow minimally invasive and robotically assisted surgical approaches in situations where currently open surgical approaches are required. Furthermore, SERRS nanoparticles naturally accumulate in the reticuloendothelial system (RES), which has enabled advances in the intraoperative imaging of cancers involving the liver and lymph nodes [16-18].

Although SERRS imaging has many advantages, it does not allow for preoperative surgical planning. Moreover, the high-resolution SERRS imaging necessary to observe small cancerous deposits limits the amount of tissue that can be imaged in an acceptable time frame during surgical procedures. These challenges can be overcome by the introduction of a complementary whole-body imaging modality that enables rapid pre-operative scans to serve as a roadmap to localize the macroscopic distribution of the tumors deep within organs. Given the very low injected dose of SERRS nanoparticles (<100 fmol/g), the most important consideration in a complementary whole-body imaging modality is the limit of detection. Thus, positron emission tomography (PET), which has a sensitivity in the range of  $10^{-11}$  –  $10^{-12}$  M, would represent an ideal complementary imaging modality for SERRS nanoparticles [19].

*In vivo* imaging of PET-active SERRS nanoparticles (PET-SERRS NPs) for clinical applications has not yet been demonstrated. A previous report of Raman nanoparticle radiolabeling describes the attachment of  $^{64}\text{Cu}$  to silica via a molecular chelator, but did not demonstrate the serum stability of the radiolabeled probe [20]. We note that  $^{64}\text{Cu}$  can attach to silica under conditions similar to those reported by the authors, albeit weakly with poor serum stability [21]. Thus, competition for radionuclide binding by the nanoparticle itself complicates efforts to perform traditional molecular-based chelation and requires further characterization to demonstrate stable radiolabeling.

The conventional molecular approach to radionuclide chelation presents several additional difficulties. First, the coordination chemistry changes significantly for different radionuclides, such that a molecule which chelates one species may fail to chelate many others. Moreover, some isotopes do not currently have established, reliable molecular chelators [22]. Secondly, the nanoparticles may not be stable under the conditions necessary for molecular chelation of radioisotopes, such as high temperatures and low or high pH. Even when a molecular chelator can be incorporated onto a nanoparticle surface, undesired side effects may occur, such as changes to the nanoparticle pharmacokinetics. Furthermore, the molecular chelators can be stripped from the nanoparticle surface *in vivo*, such that the imaging (e.g., positron emission tomography, single-photon emission tomography, etc.) and biodistribution studies do not correspond to the true distribution of the nanoparticles [23, 24]. In principle, these shortcomings could be overcome by a suitable chelator-free approach to SERRS nanoparticle radiolabeling, but to our knowledge no such method currently exists.

Chelator-free intrinsic radiolabeling has been demonstrated in various systems, such as iron oxide and metal nanoparticles. Established approaches to intrinsic radiolabeling include direct synthesis from radioactive precursors [25], exploitation of specific trapping effects [26, 27], heterogeneous cation exchange reactions [28], and heat-induced coordination of radioactive metal cations [29, 30]. We recently showed that silica nanoparticles (*i.e.*, without a gold core and free of molecular chelators) can bind  $^{89}\text{Zr}$ ,  $^{68}\text{Ga}$ ,  $^{90}\text{Y}$ ,  $^{111}\text{In}$ ,  $^{177}\text{Lu}$ , and  $^{64}\text{Cu}$  with stability proportional to the oxophilicity of the radiometal ion [31]. Subsequently, we demonstrated that the addition of sulfur to silica nanoparticle surfaces allows stable radiolabeling of softer, more thiophilic radiometal ions such as  $^{64}\text{Cu}$  [21]. Chelator-free radiolabeling has also been demonstrated with mesoporous silica nanoparticles by others [32]. Accordingly, we hypothesized that intrinsic radiolabeling of our SERRS nanoparticles could be achieved by optimizing for incorporation of radionuclides into the silica shell.

We identified the short-lived PET tracer  $^{68}\text{Ga}$  ( $t_{1/2}$  = 68 min) as the ideal candidate for the radiolabeling of SERRS nanoprobables, due to i) its oxophilicity, ii) the fact that it is readily available from commercial generators, and iii) its relatively low radiation dose to healthy tissue resulting from its short half-life [31, 33]. The consideration of radiation dose to healthy tissue is particularly important for nanoparticle imaging agents because nanoparticle preparations are sequestered to a significant degree by the RES [34].

Because of the short circulation time of these nanoproboscopes,  $^{68}\text{Ga}$  is optimal for imaging at the relevant pharmacokinetic time points (i.e. out to 3 hours). The 68-minute half-life ensures that  $^{68}\text{Ga}$  is sufficiently decayed over the course of eight hours to allow SERRS imaging intraoperatively without the potential issue of exposure to radioactivity. We note, however, that the ideal radionuclide will vary depending upon the application, and that consideration of the half-life, mechanism of decay (e.g., positron emission necessary for PET), expected dose to healthy or diseased tissue, and coordination chemistry is necessary.

## Results and Discussion

We first attempted to radiolabel SERRS nanoparticles with  $^{68}\text{Ga}$  by directly applying the protocol we had established using pure silica nanoparticles [31]. The SERRS nanoparticles consist of a gold core of ~60 nm diameter, which is coated with a Raman reporter dye and a ~30 nm thick silica shell [3, 4]. We hypothesized that exposure to  $^{68}\text{Ga}$  under the proper reaction conditions would generate intrinsically radiolabeled SERRS nanoparticles with  $^{68}\text{Ga}$  distributed throughout the silica shell (Fig. 1, 2). We performed a purified elution of  $^{68}\text{Ga}$  from the  $^{68}\text{Ge}/^{68}\text{Ga}$  generator with 0.2 N HCl followed by  $^{68}\text{Ga}$  trapping on a cartridge, which was then eluted after washing using 0.5 M potassium hydroxide (KOH). This was followed by neutralization with hydrochloric acid (HCl) or glacial acetic acid to achieve pH = 7.0-7.5 [35]. In contrast to our previous

work with pure silica nanoparticles, the silica shell of SERRS nanoparticles became extremely porous and even disintegrated entirely for some nanoparticles upon exposure to the  $^{68}\text{Ga}$  solution (Fig. S1). Consequently, the radiolabeling was unsuccessful.

The decreased stability of the SERRS nanoparticle silica shell compared to a pure silica nanoparticle is likely a consequence of their different synthetic conditions. In order to selectively generate silica shells around gold nanoparticles, the homogeneous nucleation of silica must be sufficiently disfavored such that heterogeneous nucleation and growth (i.e., shell formation) occurs, but formation of free silica nanoparticles is minimized. This is achieved by decreasing the rate of hydrolysis and condensation of silica precursors, for example by decreasing the water concentration during synthesis [36]. Decreased hydrolysis rates lead to more Si-O-Si broken bonds in the early stages of silica oligomerization and densification because the ethoxy groups of tetraethyl orthosilicate (TEOS) are not completely hydrolyzed [37-39]. Accordingly, homogenous nucleation is slow, but the gold nanoparticles provide surfaces to catalyze the condensation and aggregation reactions at the beginning of silica formation, thus enabling preferential nucleation (Fig. S2). However, the incomplete hydrolysis of silica precursors leads to broken Si-O-Si bonds within the amorphous silica structure and greater susceptibility to degradation [38]. Strategies must be developed, therefore, to render the radiolabeling procedure less harsh.

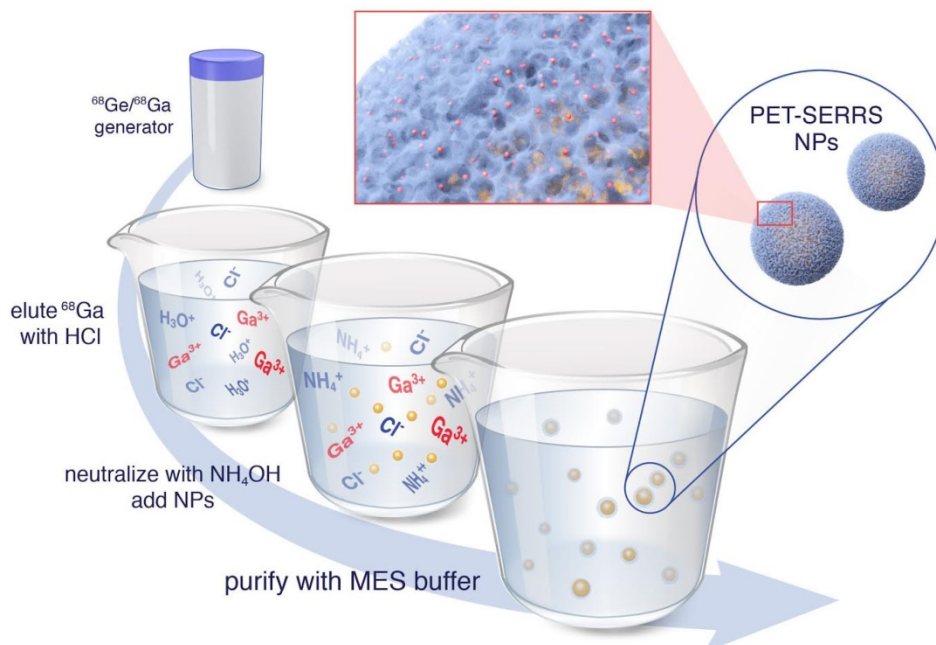


**Figure 1. Chelator-free radiolabeling of SERRS nanoparticles.**  $^{68}\text{Ga}^{3+}$  is obtained from a  $^{68}\text{Ge}/^{68}\text{Ga}$  generator via direct elution with HCl, rather than purified elution in KOH. The eluent is neutralized by addition of  $\text{NH}_4\text{OH}$  with the hypothesized net effect that  $\text{K}^+$  cations that catalyze silica dissolution are replaced by  $\text{NH}_4^+$  cations that leave the silica shells intact. The  $^{68}\text{Ga}$ -labeled PET-SERRS NPs are then easily purified by centrifugation.

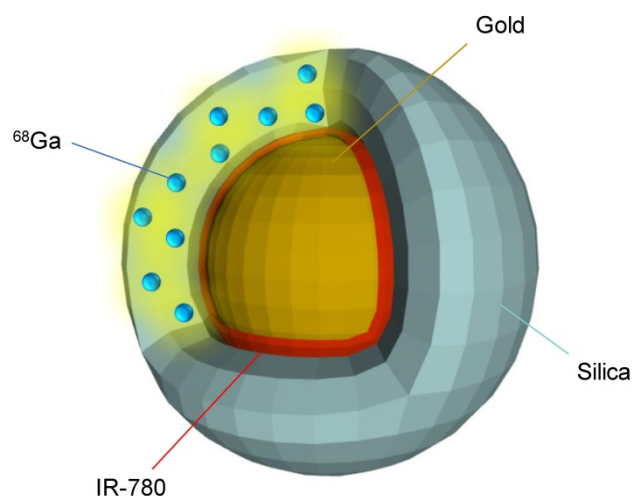


**Figure 2. Schematic of a resulting PET-SERRS nanoparticle.** The PET-SERRS nanoparticle is comprised of a gold nanoparticle core, an adsorbed layer of Raman active molecules (IR-780), and a silica shell with a radionuclide ( $^{68}\text{Ga}$ ) embedded throughout.

Since the rate of silica dissolution is catalyzed by the presence of potassium ions, we hypothesized that a radiolabeling procedure free of potassium would be less damaging to the silica shells [40]. Rather than eluting the  $^{68}\text{Ga}$  generator followed by  $^{68}\text{Ga}$  trapping on a cartridge and subsequent elution with KOH, we directly eluted the generator with 0.1 N HCl and neutralized the eluent with ammonium hydroxide ( $\text{NH}_4\text{OH}$ ) (see Methods for details) (Fig. 1). Because the  $\text{NH}_4^+$  cations are softer and bulkier than  $\text{K}^+$ , we hypothesized that they would not intercalate into the silica matrix as well; additionally, the ionic strength of the  $^{68}\text{Ga}$  solution is decreased using this strategy. The SERRS nanoparticles (10 nM nanoparticle concentration,  $3.52 \times 10^9$  g/mol molar mass, 100  $\mu\text{L}$ , pH = 8.5) were incubated with the  $^{68}\text{Ga}$  solution (100  $\mu\text{L}$ , 37 MBq (1.0 mCi), pH = 7.0-7.5) for 45 minutes at 70  $^\circ\text{C}$ , then characterized by instant thin layer chromatography (iTLC), size exclusion (SE) filtration, transmission electron microscopy (TEM), dynamic light scattering, and zeta potential analysis. Radiolabeling was tested at pH = 7.4 as well as pH = 8.5 and compared to a free  $^{68}\text{Ga}$  control that contained no nanoparticles. The radiochemical yield (non-decay corrected) was  $90.92 \pm 1.56\%$  and  $95.14 \pm 3.43\%$  for pH = 7.4 and pH = 8.5, respectively, while the molar activity was 20-100 Ci/ $\mu\text{mol}$  of NPs. Radiochemical yield was calculated as the amount of radioactivity bound to the NP after purification via centrifugal pelleting over the total radioactivity (supernatant plus NP radioactivity). These controls are necessary, as macroscale gallium solutions at neutral pH may result in colloid formation; however, radiochemical (i.e. < nanomolar) concentrations of gallium in buffer precludes colloid formation [41].

Comparison of TEM images before and after radiolabeling revealed that the stability of the silica shells was greatly improved compared to the prior radiolabeling procedure which included the presence of  $\text{K}^+$  ions (Fig. 3A-B vs. Fig. S1). However, the porosity of the silica still increased and the shell thickness decreased by approximately 7 nm according to dynamic light scattering (Tables S1, S2). Nonetheless, the intensity of the SERRS spectrum did not decrease and the  $^{68}\text{Ga}$  radioactivity remained associated with the nanoparticles (Fig. 3C-D, Fig. S3). Although iTLC suggested a minor degree of  $^{68}\text{Ga}$  detachment after 3 h in 50 % fetal bovine serum (Fig. 3D), the overall stability of the radiolabeling was sufficient to move forward with *in vivo* experiments. We note that successful radiolabeling with  $^{68}\text{Ga}$  was achieved at 25  $^\circ\text{C}$  after only 5 minutes of incubation with SERRS nanoparticles (Fig. S4), but did not demonstrate sufficient lasting stability of radiolabeling so the 70  $^\circ\text{C}$ /45 minutes-protocol was used for the remainder of the experiments.

The PET-SERRS NPs were evaluated *in vivo* by lymph node imaging near the periphery of an orthotopic 4T1 breast cancer tumor. Lymph node imaging is especially important for the identification of sentinel lymph nodes, which are routinely excised and examined by pathology in clinical practice to determine if lymphatic metastases exist [10]. Because the location of the primary draining lymphatic vessel cannot be determined by visual inspection, sentinel lymph node imaging is performed clinically by injection of a contrast agent in and around a tumor [42]. We previously showed that both radiolabeled silica nanoparticles and SERRS NPs can identify sentinel lymph nodes separately [31, 43], but the combined pre- and intra-operative imaging with a single PET-SERRS imaging agent has not yet been demonstrated. The PET-SERRS NPs were injected subcutaneously at the tumor periphery and into the tumor itself. PET imaging 4 h post-injection revealed that much of the signal remained concentrated near the tumor, suggesting that most of the PET-SERRS nanoparticles had not migrated from the injection site. Notably, the cervical lymph node can be visualized using both PET and Cerenkov imaging with strong contrast at the 4 h time point (Fig. 4A, Fig. S5). As Cerenkov luminescence (CL) intensity correlates with the velocity of the charged particle, the high positron energy of  $^{68}\text{Ga}$  ( $\beta_{\text{max}} = 1.9$  MeV) results in greater CL compared to radionuclides such as  $^{18}\text{F}$  [44, 45]. Although the axillary LN is the sentinel node for murine breast tissue, the size and location of the implanted tumor obscures the axillary LN in the small anatomical dimensions of a mouse. The cervical LN drains multiple regions, including the upper

extremities. The accumulation of PET-SERRS nanoparticles in the cervical LN occurs because one or more peripheral injection sites falls into its draining pathway [46, 47]. The cervical LN imaging illustrates that LN tracking can be achieved *in vivo* with PET-SERRS NPs.

Intraoperative imaging of the cervical LN confirmed the presence of PET-SERRS NPs via Raman spectroscopy. The characteristic Raman spectrum of the PET-SERRS nanoparticles is detectable with a handheld Raman scanner (Figure 4B, C) [6], and enables near real-time analysis of the presence of PET-SERRS NPs. Using the handheld scanner, we identified the presence of the PET-SERRS NP fingerprint spectrum in the regions that also exhibited PET contrast, confirming that the PET-SERRS nanoparticles remained intact after subcutaneous injection and migration through the lymphatic channels. The handheld Raman scanner was used to guide surgical resection of the cervical LN, first by

locating it *in vivo*, and then by confirming that all SERRS-positive tissue had been removed. Post-operative SERRS imaging was performed with the Raman imaging system to corroborate the handheld scanner results, and indeed showed that the lymph node had been completely resected (Fig. S6).

Because the PET-SERRS nanoparticles naturally accumulate in the RES, they should be well suited for imaging cancers of the liver. In particular, the high uptake of nanoparticles in healthy RES tissue and comparatively much lower uptake of nanoparticles in cancerous tissue has proven sufficient to delineate tumors *in vivo* [48, 49]. Because the cancerous regions should contain fewer PET-SERRS NPs than the surrounding liver tissue, the presence of cancer is expected to manifest in filling defects (i.e., regions of little to no signal, surrounded by regions of high signal) with both PET and SERRS imaging. A first proof-of-principle of this concept for non-radiolabeled SERRS nanoparticles was recently shown [16].

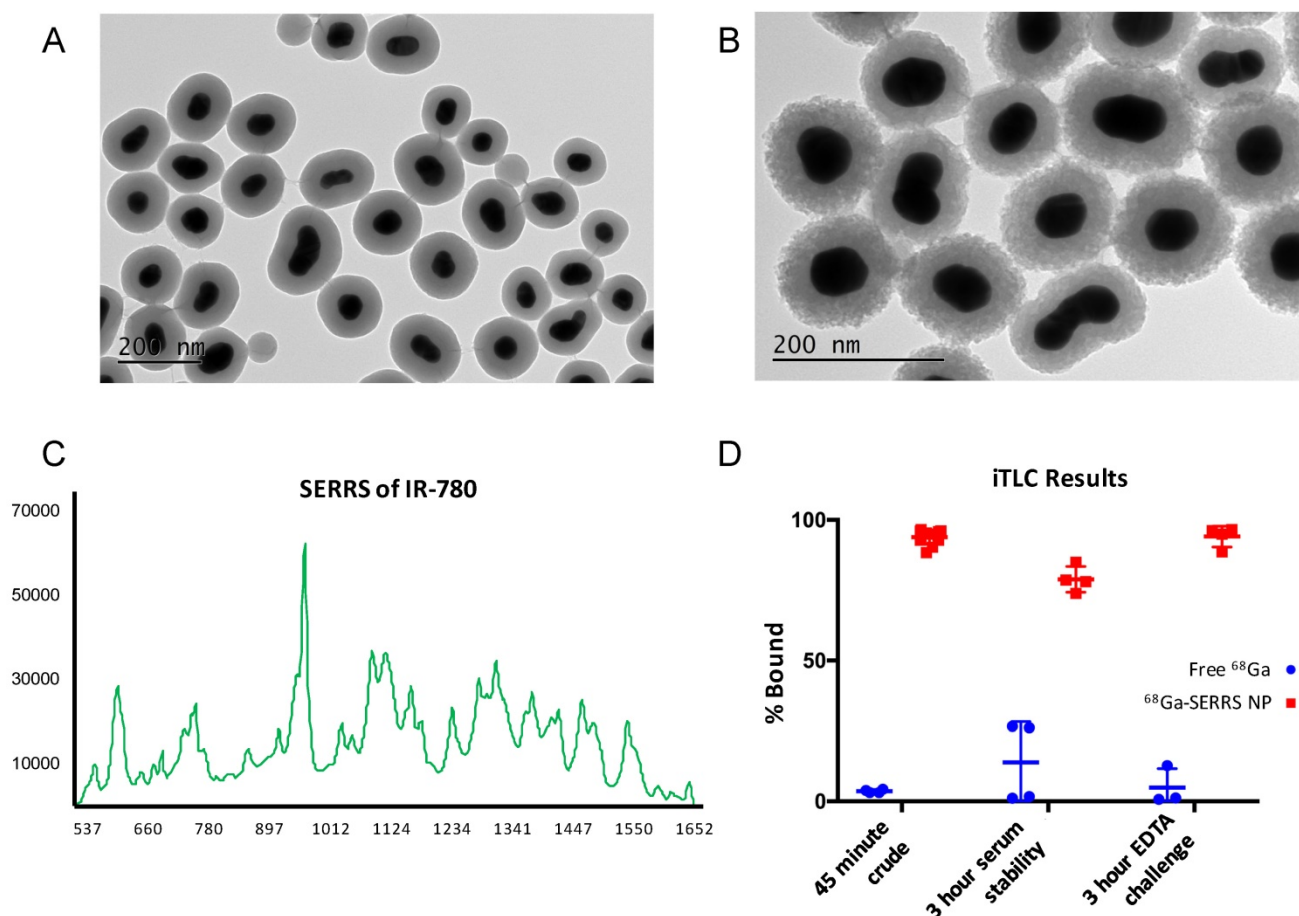


**Figure 3. Characterization of PET-SERRS nanoprobles.** (A) Transmission electron microscopy image of PET-SERRS nanoparticles before radiolabeling with <sup>68</sup>Ga. (B) Transmission electron micrograph of PET-SERRS nanoparticles after radiolabeling with <sup>68</sup>Ga at 70 °C for 45 minutes. (C) SERRS spectrum of PET-SERRS nanoparticles after radiolabeling at 70 °C for 45 minutes. The characteristic profile of IR-780 is unchanged and the intensity has not decreased. (D) Instant thin layer chromatography results of SERRS nanoparticle radiolabeling compared to free <sup>68</sup>Ga. The percentage of <sup>68</sup>Ga bound is determined by integrating the signal at the origin and dividing by the total integrated signal (see methods).

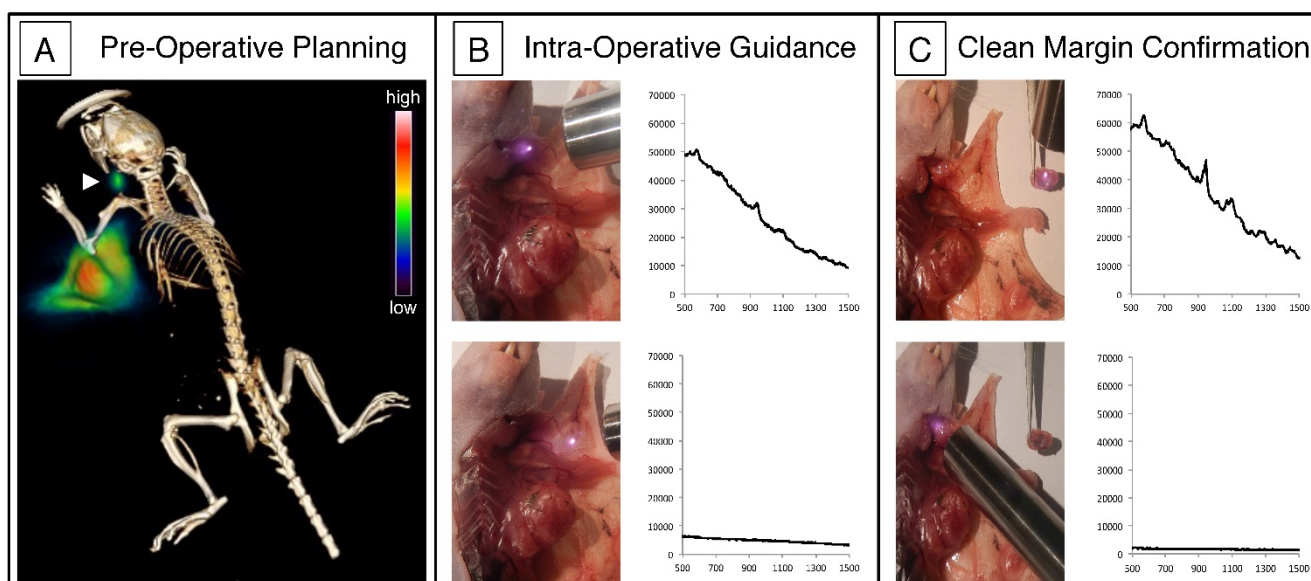


**Figure 4.** Lymph node tracking with PET-SERRS nanoparticles. **(A)** PET-CT image 4 h after the  $^{68}\text{Ga}$ -labeled PET-SERRS nanoparticles were injected around the periphery of an orthotopic 4T1 breast tumor. A lymph node can be clearly visualized away from the injection sites (arrowhead). **(B)** SERRS spectrum of PET-SERRS nanoparticles can be tracked *in vivo* with a handheld Raman scanner. The cervical LN exhibits the characteristic Raman spectrum of the PET-SERRS nanoparticle, which are not present outside of the LN. Accordingly, a quick handheld scan can be performed to guide location and resection of the LN. **(C)** After resection, the handheld scanner can be used to confirm that the SERRS spectrum is only detected in the excised tissue, indicating clean margins in the resection bed.

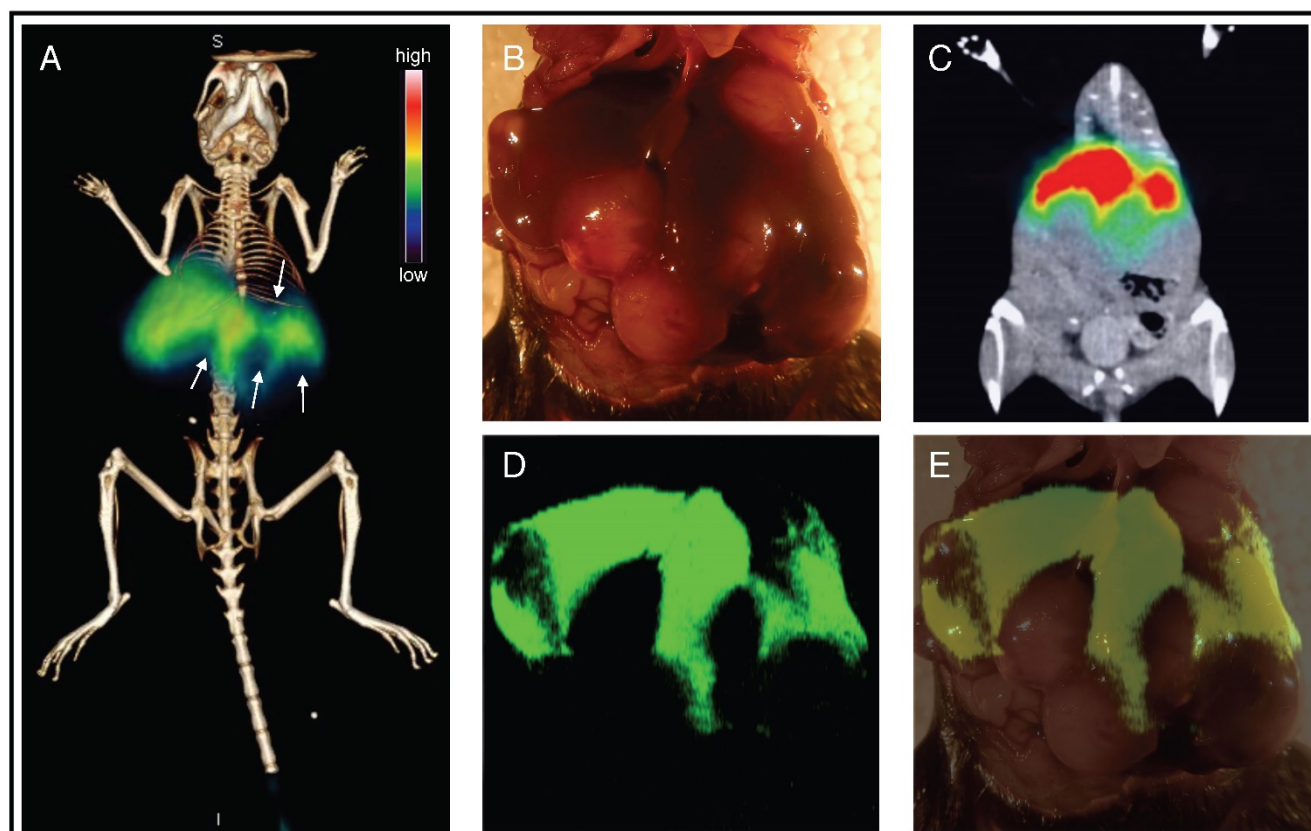


**Figure 5.** Pre-operative staging and intraoperative imaging of liver cancer using PET-SERRS nanoparticles. **(A)** PET-CT image of tumor-bearing mouse reveals clear filling defects in the liver (arrows) after injection with PET-SERRS nanoparticles. **(B)** Intraoperative white light image of the liver from the mouse imaged in **(A)**. Some of the tumors are visible by naked eye due to their large size and differential color. The location of the tumors matches the filling defects of the PET scan. **(C)** Maximum intensity projection (MIP) of the PET imaging data, showing healthy liver (high signal) and filling defects corresponding to tumors. **(D)** SERRS imaging of the liver provides a high-resolution, intraoperative map of normal liver (high SERRS signal) and location and extent of the tumors (signal voids). The correlation between PET signal and SERRS signal indicates that the nanoparticles remain intact and active *in vivo*. **(E)** Overlay of photograph and SERRS map shows that the filling defects in the SERRS signal correspond to cancer.

In order to test whether or not the  $^{68}\text{Ga}$  would remain bound to the SERRS NPs *in vivo* after intravenous injection, we injected a wild type mouse with PET-SERRS NPs (150  $\mu\text{L}$ , 10 nM nanoparticles, 500  $\mu\text{Ci}$ , 18.5 MBq  $^{68}\text{Ga}$ ) and followed the distribution of PET signal on positron emission tomography-computed tomography (PET-CT). After only 5 minutes, the PET signal was already localized to the liver according to PET-CT (Fig. S7). This concentration of PET signal in the liver is consistent with the observed biodistribution of SERRS nanoparticles and with the biodistribution of  $^{68}\text{Ga}$ -labeled silica nanoparticles [4, 31]. Moreover, this signal distribution is not consistent with the biodistribution of free  $^{68}\text{Ga}$  (i.e., not bound by a chelator), which shows high blood and bladder signal and relatively low RES signal at 1 and 3 hours post-injection [31]. Thus, the PET-CT results indicate that the  $^{68}\text{Ga}$  remains sufficiently well bound to the SERRS nanoparticles *in vivo*.

To evaluate the utility of PET-SERRS NPs for delineating liver cancers, we injected them into a mouse that had been genetically engineered to develop hepatocellular carcinomas (HCC) [16]. PET-SERRS NPs (150  $\mu\text{L}$ , 10 nM nanoparticles, 500  $\mu\text{Ci}$ , 18.5 MBq  $^{68}\text{Ga}$ ) were intravenously injected into the tail vein and PET and Cerenkov scans were obtained 3 h post-injection (Fig. 5A, Fig. S8). The PET signal exhibited several distinct filling defects throughout the liver, as hypothesized, suggesting the presence of tumors. We surgically exposed the livers of the cancer-bearing mouse and performed high-resolution SERRS scans in a simulated intraoperative setting. Even without SERRS contrast, some large tumors with sizes and locations corresponding to the filling defects on the PET scan were clearly visible. The SERRS map demonstrated pronounced filling defects where tumors were present, and correlated precisely with the pre-operative PET images (Fig. 5B-E). The co-registration of PET and SERRS signals in the liver indicate that the PET-SERRS nanoparticles remain intact after intravenous injection and circulation. To ensure that the PET signal corresponded with the healthy tissue throughout the volume of the liver, we also performed PET-MRI scans. The filling defects (i.e., negative contrast) observed via PET matched abnormal signal caused by the tumors on MRI, confirming that the PET-SERRS NPs delineate healthy versus cancerous tissue throughout the liver (Fig. 6A-C).

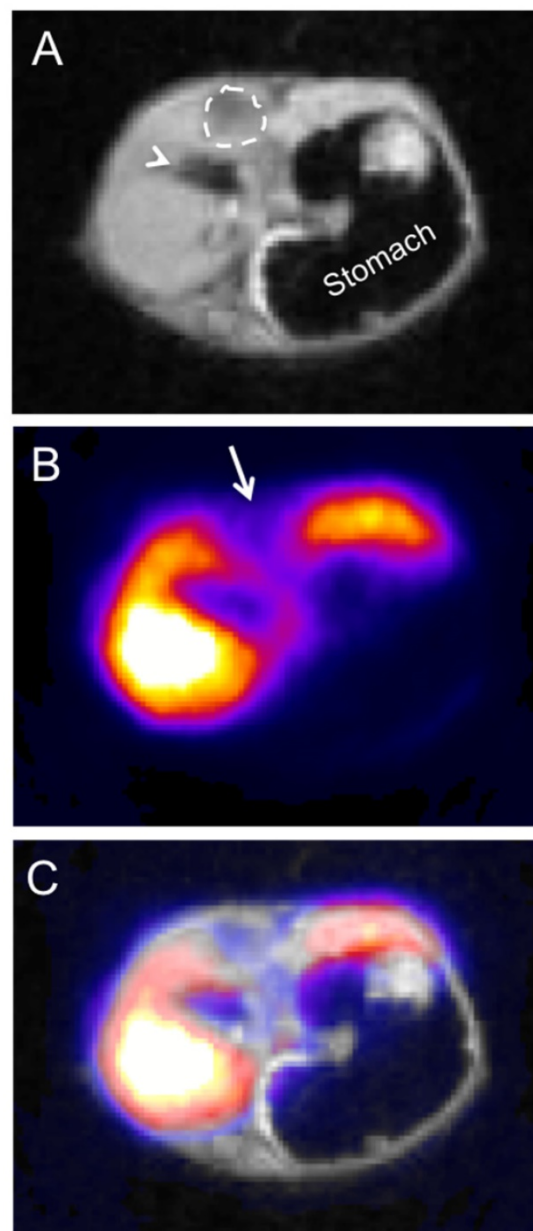


**Figure 6. PET-MR imaging of liver cancer using PET-SERRS nanoparticles.** A mouse with genetically engineered hepatocellular carcinoma (HCC) was injected with 400  $\mu\text{Ci}$  of  $^{68}\text{Ga}$ -labeled PET-SERRS NPs. After 3 hours, micro-PET-MRI was performed, and data analysis and PET-MRI co-registration were completed using VivoQuant™ software (InviCro LLC, Boston, USA). Shown are axial sections through the upper abdomen. A) Axial T1-weighted MR image through the liver, demonstrating a hypointense region (dashed-line circle), which was later confirmed to represent a HCC on pathological examination. Arrowhead = gallbladder. B) PET image with a signal void (arrow) corresponding to the location of the HCC. C) MRI-PET overlay.

## Conclusion

The stability of the PET-SERRS NPs reported herein, and their utility for *in vivo* imaging justify further investigation into their use as whole-body, combined pre- and intra-operative multimodal contrast agents. The PET-SERRS NPs enable whole-body imaging as a pre-operative roadmap and

intraoperative rapid hand-held SERRS scanning or high-resolution SERRS imaging for precise surgical guidance. Notably, this method is likely to work with a variety of other radionuclides, as observed for pure silica nanoparticles. Most importantly, this work introduces a general method for chelator-free radiolabeling of silica-encapsulated materials, thus opening many new avenues for their use in biomedical and other fields. Future research efforts will seek to improve upon the stability of the silica shells, such that no morphological changes are observed after radiolabeling. This will improve confidence that nanoparticle formulations with surface-bound species like antibodies will maintain their composition.

## Materials and Methods

### SERRS nanoparticle synthesis

Gold nanoparticles were synthesized by adding 7.5 mL 1% (w/v) sodium citrate to 1.000 L boiling 0.25 mM HAuCl<sub>4</sub>. After the nanoparticle dispersion reaches the red color indicative of a complete reaction, it is left to cool for 30 minutes, then concentrated by centrifugation (10 min, 7500 × g, 4°C) and dialyzed overnight (3.5 kDa MWCO; 5 L 18.2 MΩ·cm). The dialyzed gold nanoparticles (140 μL; 2.0 nM) were added to 1 mL absolute ethanol in the presence of 50 μL tetraethoxyorthosilicate (Sigma Aldrich, 99.999%), 20 μL 28% (v/v) ammonium hydroxide (Sigma Aldrich) and 2 μL IR-780 dissolved in N,N-dimethylformamide. IR-780 was selected because of its resonance with the 785nm laser line, cationic charge, compatibility with silication, and consistency with our previous studies. After 25 minutes of shaking (375 rpm) at ambient conditions in a plastic container, the SERRS-NPs were centrifuged, washed three times with ethanol, and redispersed in water to yield 5 nM SERRS-Nanoprobes.

### SERRS nanoparticle characterization

Nanoparticles were imaged by transmission electron microscopy (TEM) acquired on carbon grids (Ted Pella, Inc.) using a JEOL 1200 EX microscope (Peabody, MA). Dispersion concentrations were determined by Nanoparticle Tracking Analysis (NTA; Nanosight, Duxbury, MA). For radiochemical yield and serum stability studies see supporting information.

### Radiolabeling protocol

<sup>68</sup>Ga ( $t_{1/2}=68$  m) was eluted from a <sup>68</sup>Ge-<sup>68</sup>Ga generator (ANSTO, Australia) as previously described [35], with 555-740 MBq (15-20 mCi) radioactivity per elution. <sup>68</sup>Ga was eluted with 0.1 N HCl (1.5 mL), and either immediately used or trapped

on a filter, washed, and eluted with 0.5 M KOH (0.500 mL). The <sup>68</sup>Ga HCl solution was neutralized with 28% NH<sub>4</sub>OH (13 μL) while the <sup>68</sup>Ga hydroxide solution was neutralized with concentrated HCl (20-30 μL). Upon neutralization, 50-100 μL of 37 MBq (0.5-1.0 mCi) <sup>68</sup>Ga was immediately added to SERRS nanoparticle dispersions (10 nM, in 100 μL of 10 mM buffer, pH = 7.4 or pH=8.5) and incubated at 70 °C on a thermomixer at 500 rpm for 45 minutes. Purification was completed by centrifugation at 10,000 rpm for 120 seconds, followed by decanting the supernatant and redispersing in buffer (e.g. 2-(N-morpholino) ethanesulfonic acid).

### In vivo experiments

All animal experiments were done in accordance with protocols approved by the Institutional Animal Care and Use Committee of Memorial Sloan Kettering Cancer Center and followed National Institutes of Health guidelines for animal welfare.

### Genetically engineered hepatocellular carcinoma (HCC) mouse model

To generate endogenous HCCs in mice, a sterile 0.9% NaCl solution/plasmid mix was prepared containing 5 μg of DNA for the pT3 EF1a-Myc Sleeping-beauty transposon plasmid mixed with CMV-SB13 Sleeping-beauty transposase plasmid (1:5 ratio) for each injection. A total volume of the plasmid mix corresponding to 10% of body weight was injected into the lateral tail vein of eight to ten week old female FVBN mice (Jackson laboratory, Bar Harbor, USA) in 5–7 s. The pT3 transposon vector was a kind gift by Dr. Xin Chen (UCSF). Approximately 7 weeks after injection, numerous tumors were observed in the livers. Pathological examination confirmed that the tumors represented poorly differentiated HCCs.

### PET/CT imaging

At predetermined time points (1h, 3h) animals were anesthetized with isoflurane (Baxter Healthcare, Deerfield, IL) and oxygen gas mixture (2% for induction, 1% for maintenance) and scans were then performed using an Inveon PET/CT scanner (Siemens Healthcare Global). Whole body PET static scans were performed recording a minimum of 50 million coincident events, with durations of 10-30 min. The energy and coincidence timing windows were 350–750 keV and 6 ns, respectively. The image data were normalized to correct for non-uniformity of response of the PET, dead-time count losses, positron branching ratio, and physical decay to the time of injection, but no attenuation, scatter, or partial-volume averaging correction was applied.

Images were analyzed using ASIPro VMTM software (Concorde Micro-systems). Whole body standard low magnification CT scans were performed with the X-ray tube setup at a voltage of 80 keV and current of 500  $\mu$ A. The CT scan was acquired using 120 rotational steps for a total of 220 degrees yielding and estimated scan time of 120 s with an exposure of 145 ms per frame.

### Cerenkov luminescence imaging

Mice were anesthetized as described previously. Open filters were used for optical scans. 120-300 s scans were completed, depending on the photon flux.

### Handheld SERRS detection

All handheld Raman measurements were performed using the MiniRam Raman handheld scanner (B&W TEK, Inc., Newark, DE) equipped with a 785 nm laser.[6, 10] Raman spectra were collected with an acquisition time of 1 s and analyzed with B&WSpec 4.01.26 Software (B&W TEK).

### Fixed-microscope SERRS imaging

All fixed Raman scans were performed using a Renishaw inVia Raman microscope with a 300mW 785 nm diode laser and 1-inch charge-coupled device detector (1.07  $\text{cm}^{-1}$  spectral resolution). The SERRS spectra were collected with a 5 $\times$  objective (Leica) and the laser output measured at the objective was 100 mW at 100% laser power. Scans were typically performed at 100 mW laser power, 1.5-s acquisition time, using the StreamLine high-speed acquisition mode. The Raman maps were generated by means of a DCLS algorithm (WiRE 3.4 software, Renishaw).

### PET-MRI

A mouse with genetically engineered hepatocellular carcinoma (HCC) was injected with 400  $\mu$ Ci of  $^{68}\text{Ga}$ -labeled PET-SERRS NPs. After 3 hours, micro-PET-MRI was performed (T1-weighted) on a nanoScan PET/MRI system (Mediso USA, Boston, MA) and the data analysis and PET-MRI co-registration were completed using VivoQuant<sup>TM</sup> software (InviCro LLC, Boston, USA).

### Acknowledgements

The Australian Nuclear Science and Technology Organisation (ANSTO) is acknowledged for their generous provision of a research-grade gallium-68 generator and purification system. We also thank Ryan Lanning and Julio Alvarez for assistance with PET-MRI and the Kircher lab members for critical review of the manuscript. This study was funded in part by the following grants (to M.F.K.): NIH R01 EB017748 and K08 CA16396; Pershing Square Sohn Prize by the Pershing Square Sohn Cancer Research

Alliance; Center for Molecular Imaging & Nanotechnology (CMINT), Center for Experimental Therapeutics (ETC), Molecularly Targeted Intra-Operative Imaging Grant, and MSKCC Office of Technology TDF Grant; M.F.K. is a Damon Runyon-Rachleff Innovator supported (in part) by the Damon Runyon Cancer Research Foundation (DRR-29-14). The project was further supported by Mr. William H. and Mrs. Alice Goodwin and the Commonwealth Foundation for Cancer Research. M.A.W and T.M.S. were supported by a National Science Foundation Integrative Graduate Education and Research Traineeship Grant IGERT-0965983 (C.M.D). Technical services provided by the MSKCC Small-Animal Imaging Core Facility were supported in part by the MSKCC NIH Core Grant (P30 CA008748) and NIH Shared Instrumentation Grant No 1 S10 OD016207, which provided funding support for the purchase of the Inveon PET/CT.

### Supplementary Material

Supplementary figures and tables.

<http://www.thno.org/v07p3068s1.pdf>

### Competing Interests

The authors have declared that no competing interest exists.

### References

- Hockel M, Dornhofer N. The hydra phenomenon of cancer: why tumors recur locally after microscopically complete resection. *Cancer Res.* 2005; 65: 2997-3002.
- Andreou C, Kishore SA, Kircher MF. Surface-Enhanced Raman Spectroscopy: A New Modality for Cancer Imaging. *J Nucl Med.* 2015; 56: 1295-9.
- Harmsen S, Bedics MA, Wall MA, Huang R, Detty MR, Kircher MF. Rational design of a chalcogenopyrylium-based surface-enhanced resonance Raman scattering nanoprobe with attomolar sensitivity. *Nat Commun.* 2015; 6: 6570.
- Harmsen S, Huang R, Wall MA, Karabeber H, Samii JM, Spaliviero M, et al. Surface-enhanced resonance Raman scattering nanostars for high-precision cancer imaging. *Science translational medicine.* 2015; 7: 271ra7.
- Huang R, Harmsen S, Samii JM, Karabeber H, Pitter K, Holland EC, et al. High Precision Imaging of Microscopic Spread of Glioblastoma with a Targeted Ultrasensitive SERRS Molecular Imaging Probe. *Theranostics.* 2016; 6: 1075-84.
- Karabeber H, Huang R, Iacono P, Samii JM, Pitter K, Holland EC, et al. Guiding brain tumor resection using surface-enhanced Raman scattering nanoparticles and a hand-held Raman scanner. *ACS Nano.* 2014; 8: 9755-66.
- Kircher MF. How can we apply the use of surface-enhanced Raman scattering nanoparticles in tumor imaging? *Nanomedicine (Lond).* 2017; 12: 171-4.
- Nayak TR, Andreou C, Oseledchik A, Marcus WD, Wong HC, Massague J, et al. Tissue factor-specific ultra-bright SERRS nanostars for Raman detection of pulmonary micrometastases. *Nanoscale.* 2017; 9: 1110-9.
- Oseledchik A, Andreou C, Wall MA, Kircher MF. Folate-Targeted Surface-Enhanced Resonance Raman Scattering Nanoprobe Ratiometry for Detection of Microscopic Ovarian Cancer. *ACS Nano.* 2017; 11: 1488-97.
- Spaliviero M, Harmsen S, Huang R, Wall MA, Andreou C, Eastham JA, et al. Detection of Lymph Node Metastases with SERRS Nanoparticles. *Molecular imaging and biology : MIB : the official publication of the Academy of Molecular Imaging.* 2016.
- Huang X, O'Connor R, Kwizera EA. Gold Nanoparticle Based Platforms for Circulating Cancer Marker Detection. *Nanotheranostics.* 2017; 1: 80-102.
- Wall MA, Harmsen S, Pal S, Zhang L, Arianna G, Lombardi JR, et al. Surfactant-Free Shape Control of Gold Nanoparticles Enabled by Unified Theoretical Framework of Nanocrystal Synthesis. *Adv Mater.* 2017; 29.
- Harmsen S, Wall MA, Huang R, Kircher MF. Cancer imaging using surface-enhanced resonance Raman scattering nanoparticles. *Nat Protoc.* 2017; 12: 1400-14.
- Kircher MF, Josephson L, Weissleder R. Ratio imaging of enzyme activity using dual wavelength optical reporters. *Mol Imaging.* 2002; 1: 89-95.

15. Kircher MF, de la Zerda A, Jokerst JV, Zavaleta CL, Kempen PJ, Mittra E, et al. A brain tumor molecular imaging strategy using a new triple-modality MRI-photoacoustic-Raman nanoparticle. *Nature medicine*. 2012; 18: 829-34.
16. Andreou C, Neuschmelting V, Tschaharganeh DF, Huang CH, Oseledchik A, Iacono P, et al. Imaging of Liver Tumors Using Surface-Enhanced Raman Scattering Nanoparticles. *ACS Nano*. 2016; 10: 5015-26.
17. Andreou C, Pal S, Rotter L, Yang J, Kircher MF. Molecular Imaging in Nanotechnology and Theranostics. *Mol Imaging Biol*. 2017; 19: 363-72.
18. Spaliviero M, Harmsen S, Huang R, Wall MA, Andreou C, Eastham JA, et al. Detection of Lymph Node Metastases with SERRS Nanoparticles. *Mol Imaging Biol*. 2016; 18: 677-85.
19. Gambhir SS. Molecular imaging of cancer with positron emission tomography. *Nat Rev Cancer*. 2002; 2: 683-93.
20. Zavaleta CL, Hartman KB, Miao Z, James ML, Kempen P, Thakor AS, et al. Preclinical evaluation of Raman nanoparticle biodistribution for their potential use in clinical endoscopy imaging. *Small*. 2011; 7: 2232-40.
21. Shaffer TM, Harmsen S, Khwaja E, Kircher MF, Drain CM, Grimm J. Stable Radiolabeling of Sulfur-Functionalized Silica Nanoparticles with Copper-64. *Nano Letters*. 2016; 16: 5601-4.
22. Goel S, Chen F, Ehlerding EB, Cai W. Intrinsically radiolabeled nanoparticles: an emerging paradigm. *Small*. 2014; 10: 3825-30.
23. Phillips WT, Goins BA, Bao A. Radioactive liposomes. *Wiley Interdisciplinary Reviews: Nanomedicine and Nanobiotechnology*. 2009; 1: 69-83.
24. Boswell CA, Sun X, Niu W, Weisman GR, Wong EH, Rheingold AL, et al. Comparative *in Vivo* Stability of Copper-64-Labeled Cross-Bridged and Conventional Tetraazamacrocyclic Complexes. *Journal of Medicinal Chemistry*. 2004; 47: 1465-74.
25. Zhou M, Zhang R, Huang M, Lu W, Song S, Melancon MP, et al. A Chelator-Free Multifunctional [64Cu]CuS Nanoparticle Platform for Simultaneous Micro-PET/CT Imaging and Photothermal Ablation Therapy. *Journal of the American Chemical Society*. 2010; 132: 15351-8.
26. Sun Y, Yu M, Liang S, Zhang Y, Li C, Mou T, et al. Fluorine-18 labeled rare-earth nanoparticles for positron emission tomography (PET) imaging of sentinel lymph node. *Biomaterials*. 2011; 32: 2999-3007.
27. Lovell JF, Jin CS, Huynh E, Jin H, Kim C, Rubinstein JL, et al. Porphyrin nanovesicles generated by porphyrin bilayers for use as multimodal biophotonic contrast agents. *Nat Mater*. 2011; 10: 324-32.
28. Sun Y, Liu Q, Peng J, Feng W, Zhang Y, Yang P, et al. Radioisotope post-labeling upconversion nanophosphors for *in vivo* quantitative tracking. *Biomaterials*. 2013; 34: 2289-95.
29. Boros E, Bowen AM, Josephson L, Vasdev N, Holland JP. Chelate-free metal ion binding and heat-induced radiolabeling of iron oxide nanoparticles. *Chemical Science*. 2015; 6: 225-36.
30. Hoffman D, Sun M, Yang L, McDonagh PR, Corwin F, Sundaresan G, et al. Intrinsically radiolabelled [(59)Fe]-SPIONs for dual MRI/radionuclide detection. *American Journal of Nuclear Medicine and Molecular Imaging*. 2014; 4: 548-60.
31. Shaffer TM, Wall MA, Harmsen S, Longo VA, Drain CM, Kircher MF, et al. Silica nanoparticles as substrates for chelator-free labeling of oxophilic radioisotopes. *Nano Lett*. 2015; 15: 864-8.
32. Chen F, Hong H, Goel S, Graves SA, Orbay H, Ehlerding EB, et al. *In Vivo* Tumor Vasculature Targeting of CuS@MSN Based Theranostic Nanomedicine. *ACS Nano*. 2015; 9: 3926-34.
33. Kinraide TB, Yermiyahu U. A scale of metal ion binding strengths correlating with ionic charge, Pauling electronegativity, toxicity, and other physiological effects. *Journal of inorganic biochemistry*. 2007; 101: 1201-13.
34. Decuzzi P, Godin B, Tanaka T, Lee SY, Chiappini C, Liu X, et al. Size and shape effects in the biodistribution of intravascularly injected particles. *Journal of controlled release : official journal of the Controlled Release Society*. 2010; 141: 320-7.
35. Le VS. 68Ga Generator Integrated System: Elution-Purification-Concentration Integration. *Recent Results Cancer Res*. 2013; 194:43-75
36. Brinker CJ. Hydrolysis and condensation of silicates - effects on structure. *Journal of Non-Crystalline Solids*. 1988; 100: 31-50.
37. Carcouet CC, van de Put MW, Mezari B, Magusin PC, Laven J, Bomans PH, et al. Nucleation and growth of monodisperse silica nanoparticles. *Nano letters*. 2014; 14: 1433-8.
38. Keefer KD, Schaefer DW. Growth of fractally rough colloids. *Physical review letters*. 1986; 56: 2376-9.
39. Sintès T, Toral R, Chakrabarti A. Fractal structure of silica colloids revisited. *Journal of Physics a-Mathematical and General*. 1996; 29: 533-40.
40. Wijnen P, Beelen TPM, Dehaan JW, Rummens CPJ, Vandeven LJM, Vansanten RA. Silica-gel dissolution in aqueous alkali-metal hydroxides studied by Si-29-NMR. *Journal of Non-Crystalline Solids*. 1989; 109: 85-94.
41. Velikyan I. 68Ga-Based Radiopharmaceuticals: Production and Application Relationship. *Molecules*. 2015; 20: 12913.
42. Uren RF, Howman-Giles RB, Chung D, Thompson JF. Role of lymphoscintigraphy for selective sentinel lymphadenectomy. *Cancer Treat Res*. 2005; 127: 15-38.
43. Iacono P, Karabeber H, Kircher MF. A "schizophonic" all-in-one nanoparticle coating for multiplexed SE(R)RS biomedical imaging. *Angew Chem Int Ed Engl*. 2014; 53: 11756-61.
44. Gill RK, Mitchell GS, Cherry SR. Computed Cerenkov luminescence yields for radionuclides used in biology and medicine. *Physics in medicine and biology*. 2015; 60: 4263-80.
45. Shaffer TM, Pratt EC, Grimm J. Utilizing the power of Cerenkov light with nanotechnology. *Nat Nano*. 2017; 12: 106-17.
46. Hama Y, Koyama Y, Urano Y, Choyke PL, Kobayashi H. Two-color lymphatic mapping using Ig-conjugated near infrared optical probes. *J Invest Dermatol*. 2007; 127: 2351-6.
47. Zhang F, Niu G, Lu G, Chen X. Preclinical lymphatic imaging. *Mol Imaging Biol*. 2011; 13: 599-612.
48. Kumar B, Miller TR, Siegel BA, Mathias CJ, Markham J, Ehrhardt CJ, et al. Positron tomographic imaging of the liver: 68 Ga iron hydroxide colloid. *AJR Am J Roentgenol*. 1981; 136: 685-90.
49. Na HB, Song IC, Hyeon T. Inorganic Nanoparticles for MRI Contrast Agents. *Advanced Materials*. 2009; 21: 2133-48.